

# 1 Use of an Uncrewed Aerial System to Investigate Aerosol Direct and Indirect Radiative 2 Forcing Effects in the Marine Atmosphere

3  
4 Patricia K. Quinn<sup>1</sup>, Timothy S. Bates<sup>2</sup>, Derek J. Coffman<sup>1</sup>, James E. Johnson<sup>2</sup>, and Lucia M.  
5 Upchurch<sup>2</sup>

6  
7 <sup>1</sup>NOAA Pacific Marine Environmental Laboratory, Seattle, WA 98115, USA

8 <sup>2</sup>University of Washington Cooperative Institute for Climate, Ocean, and Ecosystem Studies,  
9 Seattle, WA 98105, USA

10 *Correspondence to:* Patricia K. Quinn (patricia.k.quinn@noaa.gov)

## 11 **Abstract**

12  
13 An uncrewed aerial system (UAS) has been developed for observations of aerosol and cloud properties relevant to  
14 aerosol direct and indirect forcing in the marine atmosphere. The UAS is a hybrid quadrotor – fixed wing aircraft  
15 designed for launch and recovery from a confined space such as a ship deck. Two payloads, Clear Sky and Cloudy  
16 Sky, house instrumentation required to characterize aerosol radiative forcing effects. The observing platform (UAS  
17 plus payloads) has been deployed from a ship and from a coastal site for observations in the marine atmosphere. We  
18 describe here the details of the UAS, the payloads, and first observations from the *TowBoatUS Richard L. Becker*  
19 (March 2022) and from the Tillamook UAS Test Range (August 2022). The development of this UAS technology  
20 for flights from ships and coastal locations is expected to greatly increase observations of aerosol radiative effects in  
21 the marine boundary layer over both temporal and spatial scales.

## 22 23 **1. Introduction**

24 Atmospheric aerosol particles affect the Earth’s radiation budget directly by scattering and absorbing incoming solar  
25 radiation and indirectly by taking up water and forming cloud droplets. Chemical composition of the particles  
26 determines, in part, whether they scatter incoming solar radiation back to space which leads to cooling at the Earth’s  
27 surface or absorb radiation and warm layers within the atmosphere (e.g., Li et al., 2022). The amount of heating  
28 depends on the vertical distribution of the absorbing aerosol layer, whether it is located above or below clouds, and  
29 the albedo of the surface (Takemura et al., 2002; Haywood and Ramaswamy, 1998). Whether particles act as cloud  
30 condensation nuclei (CCN) and nucleate cloud droplets depends on their size and chemical composition (Lohmann  
31 and Feichter, 2005). If the particles are large enough and contain sufficient soluble material, an increase in particle  
32 number can lead to an increase in cloud droplet number concentration and cloud albedo thereby leading to a cooling  
33 at the Earth’s surface. The degree to which aerosol direct and indirect forcing are cooling the planet and offsetting  
34 warming by greenhouse gases is highly uncertain. According to the International Panel on Climate Change (IPCC),  
35 aerosols contribute the largest uncertainty in quantifying present-day climate change (IPCC, 2021).

36 Vertical profiles of aerosol and cloud properties are required to improve models and decrease uncertainties,  
37 particularly over oceans due to the susceptibility of marine clouds to small changes in aerosol concentrations

38 (Rosenfeld et al., 2019). While satellite observations have the advantage of providing global coverage, *in situ*  
39 observations have the highest level of accuracy available to constrain radiative forcing and reduce uncertainties in  
40 forcing estimates (Li et al., 2022). Crewed aircraft have been used for the past several decades to characterize  
41 horizontal and vertical distributions of aerosol and cloud properties relevant to radiative forcing (e.g., Russell et al.,  
42 1999; Yoon and Kim, 2006; Zhang et al., 2017). These measurements come at a relatively high cost and require  
43 extensive logistical coordination.

44  
45 Uncrewed aerial systems, or UAS, have the advantage of lower costs and flexibility and frequency of flights  
46 compared to crewed aircraft. In addition, they offer higher spatial resolution due to their relatively slow flight speed.  
47 UAS have been used since the mid-2000s to measure aerosol and cloud properties relevant to radiative forcing  
48 including particle number concentration and size distribution, light absorption, aerosol optical depth, and cloud drop  
49 number and effective radius. These measurements have been made with vertical-take-off-and landing (VTOL) UAS,  
50 either quadcopters (Brady et al., 2016) or hexacopters (e.g., Chilinski et al., 2016; Aurell et al., 2017), or fixed wing  
51 UAS (Corrigan et al., 2008; Bates et al., 2013). The VTOL UAS that have been used have the advantage of not  
52 needing a catapult or runway to be launched and recovered but typically have short endurance (< 30 min) and a  
53 limited altitude ceiling (~1 km). The fixed wing aircraft that have been used require a launch and recovery apparatus  
54 or a runway but have the advantage of longer duration (hours) and can reach high altitudes of 3 km or more. While  
55 some VTOLs used can carry relatively heavy payloads (6 kg or more), they can only do so for ~ 15 min while some  
56 of the fixed wing UAS can carry heavy payloads for hours.

57  
58 We report here on measurements of aerosol and cloud properties using a hybrid quadrotor – fixed wing UAS, the  
59 Fixed Wing VTOL Rotator or FVR-55, developed by L3Harris Latitude Engineering. The hybrid quadrotor – fixed  
60 wing concept combines the advantages of fixed wing flight with the ability to take-off and land vertically thus  
61 eliminating the need for a runway and allowing for launch and recovery from ships and other confined spaces. The  
62 FVR-55 has an endurance of more than 4 hours, a height ceiling of at least 3 km, and can carry a 6 kg payload.  
63 NOAA PMEL has developed two UAS payloads -- one for the measurement of aerosol properties relevant to direct  
64 radiative forcing (Clear Sky) and one for the measurement of aerosol and cloud properties relevant to indirect  
65 forcing (Cloudy Sky). The FVR-55 and instrumentation in the two payloads are described herein along with the  
66 results of its first shipboard and coastal flights.

67

## 68 **2. Methods**

69

### 70 **2.1. FVR-55**

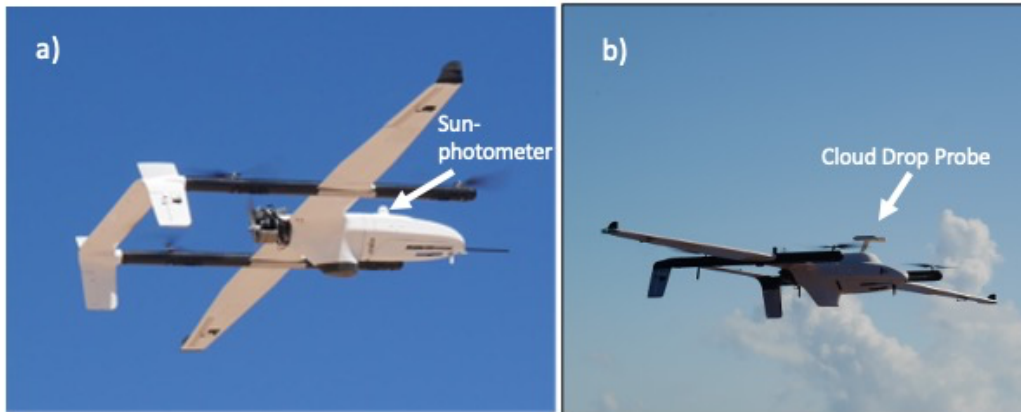
71

72 The FVR-55, a class II medium endurance UAS, was developed by Latitude Engineering (since acquired by  
73 L3Harris) with support from NOAA Phase I and II SBIRs (Small Business Innovation Research awards) (see Figure  
74 1). The focus of the SBIR was a UAS able to carry a 5.5 kg payload, have a flight ceiling of up to 3 km, an

75 endurance of 3 hrs or more, and a pusher engine. The hybrid quadrotor – fixed wing design of the FVR-55 combines  
76 the high-power density of electric motors and propellers with the high-energy density of a piston engine and liquid  
77 fuel. The electric-quadrotor system is used during launch and recovery (high power, short endurance) and the gas  
78 engine is used for fixed wing flight (low power, long endurance). The aircraft has an empty weight of 20 kg and a  
79 maximum take-off weight of 29.5 kg. It cruises at  $25 \text{ m s}^{-1}$ . A Cloud Cap Piccolo autopilot flight controller is used  
80 for autonomous flight. In the case of a lost link, the avionics guides the UAS to a predetermined return to base  
81 location and, if communication is not re-established, to land at an established target. A mobile ground control station  
82 (Windows tablet or Laptop with Datalink) provides ground command and control. A differential GPS (dGPS)  
83 system is used for computing the aircraft's heading to circumvent the challenges created by the hull of a ship  
84 distorting the Earth's magnetic field. The fuselage of the FVR-55 was designed for a maximum spacing of the two  
85 dGPS antennas to increase the accuracy of the computed heading. VTOL motors and propellers provide enough  
86 overall power for the FVR-55 to handle turbulence created by relative wind blowing over the superstructure of a  
87 ship. A “pusher engine” is used to minimize contamination of sample air in flight by exhausting the engine aft while  
88 the UAS flies forward. When the flight track includes circles or spirals engine contamination can occur but is readily  
89 identifiable by short-lived increases in particle number concentration. We removed all data during these  
90 contaminated periods. Individual payloads are integrated into a nose cone to allow for easy swapping of payloads  
91 between flights. Payloads are powered at 12VDC from the plane with 200 W of power available.

92

93 Figure 1. FVR-55 with a) Clear Sky and b) Cloudy Sky payloads onboard.



94

95

96 Table 1. Specifications of the FVR-55 UAS.

97

Cruise speed	25 m s <sup>-1</sup>
Weight with no payload or fuel	20 kg
Maximum take-off weight	29.5 kg
Endurance at maximum take-off weight including a 6.0 kg payload	4.5 hrs
Altitude ceiling	3,050 m
VTOL landing on land or ship	6 m x 6 m recover area
Size	4 m x 2.1 m x 0.3 m

98

99

100 **2.2. Payloads**

101

102 2.2.1. Inlet, sample air flow, and data acquisition

103 An isokinetic inlet is mounted on the nose cone of the FVR-55 to bring sample air into the payload under vacuum  
 104 (See Figure 2). No changes in particle number concentration coinciding with the UAS transitioning from large  
 105 spirals (1 to 2 km) to level leg flights were observed, indicating the performance of the isokinetic inlet was not  
 106 impacted by a spiral flight pattern. Since particle number concentrations are dominated by the submicron size range  
 107 this metric does not rule out effects in supermicron size ranges. In addition, the slow air speed of the UAS (25 m sec<sup>-1</sup>)  
 108 is expected to decrease impacts of the flight pattern on transmission of submicron particle through the inlet into  
 109 the payload. Wind tunnel tests are planned for the determination of the particle passing efficiency as a function of air  
 110 speed and particle size.

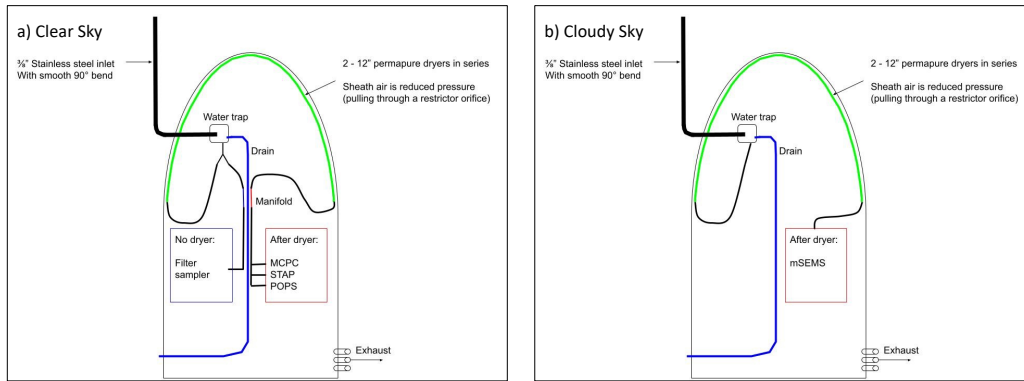
111

112 Sample air first encounters an inline water trap where water droplets are removed through impaction. The water trap  
 113 has two outlets -- one outlet is for the sample line, which is under vacuum. The larger outlet exhausts condensate  
 114 through a drain line that also allows excess ram air to passively exit the sampling system. Individual instruments  
 115 sub-sample off of the sample inlet. For the Clear Sky payload, a perma pure drier is located downstream of the water  
 116 trap and upstream of all instruments except the filter sampler (Figure 2a). For the Cloudy Sky payload, a perma pure  
 117 drier is located downstream of the water trap and upstream of the mSEMS (Figure 2b). A restricting orifice and filter  
 118 on the inlet of the perma pure sheath air combined with a vacuum on the outlet of the sheath air was used to remove  
 119 moisture from the sample stream. Instruments are cooled in flight by air flow through vent shafts cut into the nose  
 120 cone frame. More details about the instruments in each payload are provided in Sections 2.2.2. (Clear Sky) and  
 121 2.2.3. (Cloudy Sky).

122

123

124 **Figure 2. Flow diagrams for a) Clear Sky and b) Cloudy Sky payloads.**



125  
126

127 The data acquisition (DAQ) systems for the two payloads use different hardware and software but have the same  
128 functionality. The Clear Sky payload DAQ is an Arduino based system that uses Labview software to collect data  
129 and control the sensors. The Cloudy Sky payload uses a Raspberry PI running Python software to do the same. Both  
130 DAQ systems collect and save data locally (on the aircraft) and also send data back to a ground station via a Silvus  
131 radio link in near real-time. This communication link allows for command and control of the sensors during flight as  
132 well as the ability to save a second copy of the data on the ground.

133

### 134 2.2.2. Clear Sky Payload

135

136 The Clear Sky Payload was designed to measure aerosol properties required for quantification of aerosol direct  
137 radiative effects. All of the initial instruments in the payload were built by Brechtel Manufacturing Inc. (BMI,  
138 Haywood, CA; ACCESS Model 9400) under a NOAA SBIR. The payload was first flown on a MANTA C1 UAS  
139 from Ny-Ålesund, Svalbard, Norway in 2011 (Bates et al., 2013). The instruments included a mixing condensation  
140 particle counter (MCPC) for measuring total particle number, or condensation nuclei (CN) concentration; a three-  
141 wavelength Single Channel Tricolor Absorption Photometer (STAP) for measuring the aerosol light absorption  
142 coefficient; and a multi-channel filter sampler for the collection of aerosol samples for post-flight chemical analysis.  
143 Two instruments were added to the payload in 2014 including a Printed Optical Particle Spectrometer (POPS) for  
144 the measurement of particle number size distribution (0.14 to 3  $\mu\text{m}$ ) (Telg et al., 2017) and a Mini Scanning Aerosol  
145 Solar Photometer (mini-SASP) for the measurement of sun and sky radiance (Murphy et al., 2016). The payload also  
146 includes Rotronic HC2-S3 and Innovative Sensor Technology (IST) HYT271 temperature and humidity sensors.  
147 The updated version of the Clear Sky Payload was flown during a second campaign from Ny-Ålesund in 2015 (Telg  
148 et al., 2017). A perma pure drier is plumbed into the sample line to provide dried air to the MCPC, STAP, and  
149 POPS. The RH of the sampled air downstream of the drier was  $34 \pm 1.6\%$ , or  $\sim 8\%$  lower than ambient RH, for  
150 results reported here from a high-altitude flight off the coast of Oregon in August 2022. The Clear Sky Payload plus  
151 the FVR-55 nose cone weighs 6 kg. The mini-SASP mounted on top of the FVR-55 nose cone is shown in Figure  
152 1a. Table 2 lists the instruments in the Clear Sky Payload that were integrated into the FVR-55 nose cone. Sampling

153 rates were 1 sec for all real time instruments while filter samples were collected over a period of minutes to hours.  
 154 Further details on each instrument are provided below. Comparisons between Clear Sky and bench top instruments  
 155 are presented in Sect. 3.

156

157 Table 2. Measured parameters and instrumentation in the Clear Sky Payload.

Clear Sky Payload Instrumentation			
Measured Parameter	Derivable Parameter(s)	Instrument	Uncertainty
Total particle number concentration, > 0.005 $\mu\text{m}$		Brechtel Mixing Condensation Particle Counter (MCPC)	$\pm 8\%$ <sup>a</sup>
Particle number size distribution, 0.14 to 3 $\mu\text{m}$	Scattering coefficient, asymmetry parameter, Ångstrom exponent <sup>b</sup>	Portable Optical Particle Spectrometer (POPS)	$\pm 10\%$ particle concentration accuracy
Aerosol light absorption coefficient (dry) (450, 525, and 624 nm)	Absorption aerosol optical depth (AOD <sub>abs</sub> )  Single scattering albedo when paired with scattering coefficient derived from the measured number size distribution	Brechtel Single Channel Tricolor Absorption Photometer (STAP)	$\pm 33\%$ at 1.0 Mm <sup>-1</sup> , <sup>c</sup>
Sun and sky radiance (460.3, 550.4, 671.2, and 860.7 nm)	Aerosol optical depth (AOD)	Mini Scanning Aerosol Solar Photometer (mini-SASP)	0.01 detection limit (AOD)
Chemical composition (Na <sup>+</sup> , NH <sub>4</sub> <sup>+</sup> , K <sup>+</sup> , Mg <sup>2+</sup> , Ca <sup>2+</sup> , Cl <sup>-</sup> , NO <sub>3</sub> <sup>-</sup> , Br <sup>-</sup> , SO <sub>4</sub> <sup>2-</sup> )		Brechtel Multi-Channel Chemical Sampler	$\pm 5\%$ <sup>d</sup> $\pm 8.5\%$ <sup>e</sup>
T		Rotronic HC2-S3 IST HYT271	$\pm 0.1^\circ\text{C}$ (<15 s) <sup>f</sup> $\pm 0.2^\circ\text{C}$ (<15 s) <sup>f</sup>
RH		Rotronic HC2-S3 IST HYT271	$\pm 0.8\%$ (<5 s) <sup>f</sup> $\pm 1.8\%$ (<4 s) <sup>f</sup>

158 <sup>a</sup>Coincidence corrected concentration uncertainty at 10,000 cm<sup>-3</sup>

159 <sup>b</sup>Using Mie theory

160 <sup>c</sup>Bates et al. (2013)

161 <sup>d</sup>Sample flow accuracy (uncertainty due to Chemical Sampler only)

162 <sup>e</sup>Overall uncertainty for the measurement of inorganic ions

163 <sup>f</sup>Time response

164

165 The MCPC (modified BMI Model 1710) has a 0.18 s response time, grows particles in a butanol-saturated flow, and  
 166 counts particles larger than 5 nm in diameter. Modifications to the butanol handling components of the commercial  
 167 Model 1710 were implemented to address the high vibration environment of the UAS (Bates et al., 2013). The  
 168 MCPC has a  $\pm 8\%$  coincidence corrected uncertainty for a particle concentration of 10,000 cm<sup>-3</sup>.

169

170 The STAP provides real-time measurement of the aerosol light absorption coefficient at 450, 525, and 624 nm. Light  
 171 is transmitted from an LED source through a sample and a reference filter. The filter transmission is the ratio of the  
 172 signals from the two filters. The light absorption coefficient is proportional to the rate of decrease of light  
 173 transmittance divided by the flow rate of air through the filter (Bond et al., 1999). The raw data are averaged into 60

174 sec values for the calculation of the rate of decrease of light transmittance. The minimum detectable level, MDL,  
175 defined as the peak-to-peak noise with the instrument running particle free air, is  $0.2 \text{ Mm}^{-1}$ . Errors in the STAP  
176 measurement include noise in the transmission value, uncertainty in the measured flow rate, and uncertainty in the  
177 measured filter spot area (Anderson et al., 1999). A quadrature sum of these errors yields a relative uncertainty of  $\pm$   
178  $33\%$  at  $1.0 \text{ Mm}^{-1}$ . In addition, light scattering by particles collected on the sample filter can lead to an  
179 overestimation of absorption values by  $\sim 2\%$  of the observed scattering coefficient (Bond et al., 1999). A correction  
180 for scattering was not performed on the data collected in August 2022. The temperature and relative humidity of the  
181 sample air flow drawn into the STAP was  $12 \pm 1.6^\circ\text{C}$  and  $34 \pm 1.6\%$ , respectively, for conditions encountered off of  
182 the coast of Oregon in August 2022.

183  
184 The Brechtel Multi-Channel Chemical Sampler has eight filter holders (13 mm diameter) and a magnetically-driven  
185 rotary valve manifold that distributes the vacuum from a central pump to each of the sampling channels. A remote  
186 serial command is used to move the rotary valve to a new sampling channel in flight. The sample flow rate is  $2.5 \text{ L}$   
187  $\text{min}^{-1}$  which is measured by the pressure drop through a laminar flow element. One of the eight channels can be used  
188 to maintain flow when a filter sample is not being collected. 13 mm Millipore Fluoropore  $1.0 \mu\text{m}$  PTFE membrane  
189 filters were used for sample collection. For the measurements reported here, filters were extracted post-flight in a  
190  $17\%$  methanol/water solution for analysis by ion chromatography (IC). The volume of liquid used to extract the  
191 filters was minimized to  $1 \text{ mL}$  to increase the sensitivity of the method. Filters were sonicated for  $30 \text{ min}$ . The filter  
192 extract was injected into a Metrohm 940 Professional IC Vario with 889 IC Sample Center autosamplers and  
193 analyzed for inorganic cations ( $\text{Na}^+$ ,  $\text{NH}_4^+$ ,  $\text{K}^+$ ,  $\text{Ca}^{2+}$ ,  $\text{Mg}^{2+}$ ) and anions ( $\text{Cl}^-$ ,  $\text{NO}_3^-$ ,  $\text{SO}_4^{2-}$ ). A Metrosep C6 - 100/4.0  
194 column,  $2 \text{ mMol HNO}_3$  eluent, and a flow rate  $0.9 \text{ ml min}^{-1}$  were used for the cation analysis. Metrosep A Supp 5 -  
195  $250/4.0$  and Phenomenex Star Ion A300- 100/4.6mm columns in serial, a  $1 \text{ mMol NaHCO}_3$  and  $5 \text{ mMol Na}_2\text{CO}_3$   
196 eluant, and a flow rate of  $0.7 \text{ ml min}^{-1}$  were used for the anion analysis. Sources of uncertainty in the chemical  
197 analysis include air volume sampled ( $\pm 5\%$ ), the extract liquid volume ( $\pm 3.5\%$ ), 2 times the standard deviation of  
198 the blank, and precision/calibration of the method ( $\pm 5\%$ ). Total average overall uncertainty was  $\pm 8.5\%$ . Only ion  
199 concentrations above 2 times the standard deviation of the filter blank are reported here.

200  
201 Particle number size distributions from  $0.14$  to  $3.0 \mu\text{m}$  in diameter were measured with a POPS (Telg et al., 2017).  
202 The POPS detects and sizes single particles based on the dependence of the scattering intensity on particle size. A  
203  $405 \text{ nm}$  laser diode is used as a light source. The light scattering signal is collected at scattering angles between  $38^\circ$   
204 and  $142^\circ$  (Gao et al., 2016). As for the MCPC and the STAP, the temperature and RH of the sample air drawn into  
205 the POPS was  $12 \pm 1.6^\circ\text{C}$  and  $34 \pm 1.6\%$ , respectively, for conditions encountered off of the coast of Oregon in  
206 August 2022. Uncertainty for the POPS is  $\sim 10\%$  of the total particle concentration.

207  
208 Sun and sky radiance were measured with a miniSASP at wavelengths of  $460.3$ ,  $550.4$ ,  $671.2$ , and  $860.7 \text{ nm}$   
209 (Murphy et al., 2016). Four independent telescopes, each with a unique interference filter, are housed in a single  
210 aluminium block. A heater is integrated with a temperature controller to minimize condensation and keep the

211 photodiodes at an approximately constant temperature. The miniSASP scans the sky at the elevation angle of the  
212 sun. A full azimuth revolution is made in about 30 s and measurements are made every 30 ms. Sun angle is  
213 corrected for the tilt of the UAS. Each revolution of the miniSASP's telescopes results in a distinct peak  
214 corresponding to the intensity of direct sun light. The aerosol optical depth of an atmospheric layer on the slant path  
215 is the difference between the sun signal and Rayleigh scattering. Flight data from Svalbard in 2015 show a detection  
216 limit better than 0.01 in AOD for a vertical profile through the bottom few kilometers of the atmosphere.

217

### 218 **2.2.3. Cloudy Sky Payload**

219

220 The Cloudy Sky payload was designed to characterize the relationship between cloud drop number concentration  
221 and particle number concentration and size below, within, and above cloud. The Cloudy Sky payload has a Brechtel  
222 miniature Scanning Electrical Mobility Sizer (mSEMS) for the measurement of particle number size distribution  
223 (0.01 to 0.3  $\mu\text{m}$ ) and total particle number concentration. A perma pure drier is plumbed into the sample line to  
224 provide dried air to the mSEMS. The RH of the sheath air was measured during operation. The RH of the dried  
225 sample air depended on ambient conditions but ranged from 35 to 45% for the flights from Tillamook. Operating  
226 conditions for the mSEMS included a sheath flow rate of 2.5 lpm, sample flow rate of 0.36 lpm, and a size scan of  
227 30 bins at 1 sec per bin resulting in a sampling rate of 30 sec for each size distribution.

228

229 A miniature and light weight Cloud Drop Probe (DMT, CDP-2) is used to measure cloud droplet number  
230 concentration and size distribution between 2 and 50  $\mu\text{m}$ . The payload also has Rotronic HC2-S3 and IST HYT271  
231 temperature and humidity sensors. Cloudy Sky instrumentation and specifications are listed in Table 3. The Cloudy  
232 Sky payload was integrated into an FVR-55 nose cone in March 2021 at the L3Harris facility in Tucson, Arizona.  
233 The payload then flew three flights onboard the FVR-55 at the Florence Military Range up to an altitude of 2.6 km.  
234 The cloud droplet probe mounted on top of the FVR-55 nose cone is shown in Figure 1b. Further details on each  
235 instrument are provided below. Comparisons between Cloudy Sky and bench top instruments are presented in Sect.  
236 3.

237

238 The Brechtel mSEMS (Model 9404) provided particle number size distributions for diameters between 0.01 to 0.3  
239  $\mu\text{m}$  every 30 seconds. Total particle number concentration was obtained by integrating the number concentration  
240 over the measured size distribution. The RH of sample air drawn into the mSEMS was  $45 \pm 0.74\%$ , which was ~  
241 40% below ambient RH, for the conditions encountered during flights off the coast of Oregon in August 2022. As  
242 for the Clear Sky payload, the MCPC has an  $\pm 8\%$  coincidence corrected uncertainty for a particle concentration of  
243  $10,000 \text{ cm}^{-3}$ .

244

245 A DMT CDP-2 was mounted on the top of a FVR-55 nose cone for measurement of cloud drop number  
246 concentration for diameters from 2 to 50  $\mu\text{m}$  and retrieval of liquid water content. Liquid water content was derived  
247 from the cloud droplet size distribution provided by the DMT CDP-2. The CDP-2 measures cloud droplet counts



248 and sizes them into 30 bins from 2-30  $\mu\text{m}$ . The count in each bin is converted to a concentration using the cross-  
 249 sectional surface area of the sensing beam ( $0.24 \mu\text{m}^2$ ) and the speed of the aircraft to determine the volume of air  
 250 sampled per second. Once the concentration is known, the volume of cloud droplets per volume is calculated and  
 251 converted to mass per volume assuming density of 1.0.

252

253 Table 3. Measured parameters and instrumentation in the Cloudy Sky Payload

Cloudy Sky Payload Instrumentation			
Measured Parameter	Derivable Parameter(s)	Instrument	Uncertainty
Particle number size distribution and total number concentration (0.01 to 0.3 $\mu\text{m}$ in diameter)	Scattering coefficient, asymmetry parameter, Ångstrom exponent <sup>b</sup>	Brechtel miniature Scanning Electrical Mobility Sizer (mSEMS) coupled with a MCPC detector	$\pm 8\%$ <sup>a</sup>
Cloud droplet number concentration and size (2 to 50 $\mu\text{m}$ )	Cloud liquid water content Cloud droplet effective diameter	DMT miniature Cloud Drop Probe (CDP-2)	
T		Rotronic HC2-S3 IST HYT271	$\pm 0.1^\circ\text{C}^{\text{d}}$ (<15 s) <sup>b</sup> $\pm 0.2^\circ\text{C}$ (<15 s) <sup>b</sup>
RH		Rotronic HC2-S3 IST HYT271	$\pm 0.8\%^{\text{d}}$ (<5 s) <sup>b</sup> $\pm 1.8\%$ (< 4 s) <sup>b</sup>

254 <sup>a</sup>Coincidence corrected concentration uncertainty at  $10,000 \text{ cm}^{-3}$

255 <sup>b</sup>Response time

256

### 257 3. Comparison of UAS and bench top measurements

258

259 The degree of agreement between the bench and payload measurements of particle number concentration and  
 260 absorption coefficient were evaluated by calculating the relative difference between the measurements as

261

$$262 \quad \text{relative difference} = \left( \frac{x_{\text{bench}} - x_{\text{uas}}}{x_{\text{bench}}} \right) \quad (1)$$

263

264 where  $x_{\text{bench}}$  and  $x_{\text{uas}}$  are the bench and UAS measured values, respectively. The overall experimental uncertainty was  
 265 calculated as

266

$$267 \quad \text{experimental uncertainty} = [(\delta x_{\text{bench}})^2 + [(\delta x_{\text{uas}})^2]^{1/2}] / x_{\text{bench}} \quad (2)$$

268

269 where  $\delta x_{\text{bench}}$  and  $\delta x_{\text{uas}}$  are the uncertainties in the bench and UAS measurements, respectively, as reported in Tables  
 270 1 and 2 and taken from manufacturer specifications.

271

272

### 273 3.1. Particle number concentration

274

275 Particle number concentrations measured by the Clear and Cloudy Sky payloads and bench top instruments were  
276 compared during ATOMIC (The Atlantic Tradewind Ocean-Atmosphere Mesoscale Interaction Campaign), a cruise  
277 in the tropical North Atlantic (Quinn et al., 2021). The comparison took place on January 24, 2020 from 18:40 to  
278 22:00 UTC. For both the payload and the bench top instruments, sample air was drawn through a 5 m mast 18  
279 m.a.s.l. and forward of the ship's stack. The mast was automatically rotated into the wind to maintain nominally  
280 isokinetic flow. Air entered the inlet through a 5-cm diameter hole, passed through a 7° expansion cone, and then  
281 into the 20-cm inner diameter sampling mast. The flow through the mast was  $1 \text{ m}^3 \text{ min}^{-1}$ . The transmission  
282 efficiency of the inlet for particles with aerodynamic diameters  $< 6.5 \text{ }\mu\text{m}$  is greater than 95% (Bates et al., 2002).  
283 The bottom 1.5 m of the mast was heated so that the sample air was at an RH of  $60 \pm 5\%$ . Stainless steel tubes  
284 extending into the heated portion of the mast were connected to bench top instrumentation and payload inlets with  
285 conductive silicone tubing.

286

287 A bench top MAGIC210 particle counter, which measures particles with diameters greater than  $0.005 \text{ }\mu\text{m}$ , was  
288 compared to the Clear Sky MCPC and the Cloudy Sky mSEMS (Figure 3, top of plot). Differential Mobility Particle  
289 Sizers (DMPS) and an Aerodynamic Particle Sizer (APS) were used for the comparison to the Clear Sky POPS for  
290 particles with diameters greater than  $0.14 \text{ }\mu\text{m}$  (Figure 3, bottom of plot). A combination of an Aitken DMPS and an  
291 Accumulation DMPS measures the size distribution between  $0.002$  and  $0.8 \text{ }\mu\text{m}$  in geometric diameter. The APS  
292 measures the size distribution between  $0.85$  and  $10.37 \text{ }\mu\text{m}$  in aerodynamic diameter. The DMPS and APS size  
293 distributions were merged by converting the APS data from aerodynamic to geometric values using calculated  
294 densities and associated water mass at 60% RH based on the range of measured chemical compositions reported by  
295 Quinn et al. (2002). The DMPSs and APS are housed in a temperature-controlled box at the base of the inlet to  
296 maintain a uniform RH across all instruments. Given that the payloads and bench instruments were measured from a  
297 common inlet and the residence time in the tubing to the payloads was short, it is likely that RH differences in the  
298 sample air delivered to the payload and bench instruments were negligible over the comparison period. The payload  
299 data were averaged into 5-minute time periods to match the DMPS/APS scan times.

300

301 The average difference between the bench MAGIC CPC and the Clear Sky payload MCPC number concentration  
302 was  $22 \pm 42 \text{ cm}^{-3}$ , resulting in an average relative difference of  $5.2 \pm 0.9\%$ . The relative difference is smaller than  
303 the overall experimental uncertainty of  $9.5 \pm 0.09\%$  indicating good agreement. The coefficient of determination,  $r^2$ ,  
304 for the comparison was 0.99. These results indicate that the trends in the two measures of number concentration  
305 agreed well. However, the bench instrument was consistently higher by about 5%. Differences could be due to  
306 particle losses in sampling lines. Particle losses will be quantified in future experiments.

307

308 The average difference between the bench MAGIC CPC and the Cloudy Sky integrated number concentration from  
309 the mSEMS was  $-1.9 \pm 9.8 \text{ cm}^{-3}$ , resulting in an average relative difference of  $-0.19 \pm 0.67\%$ . This difference is

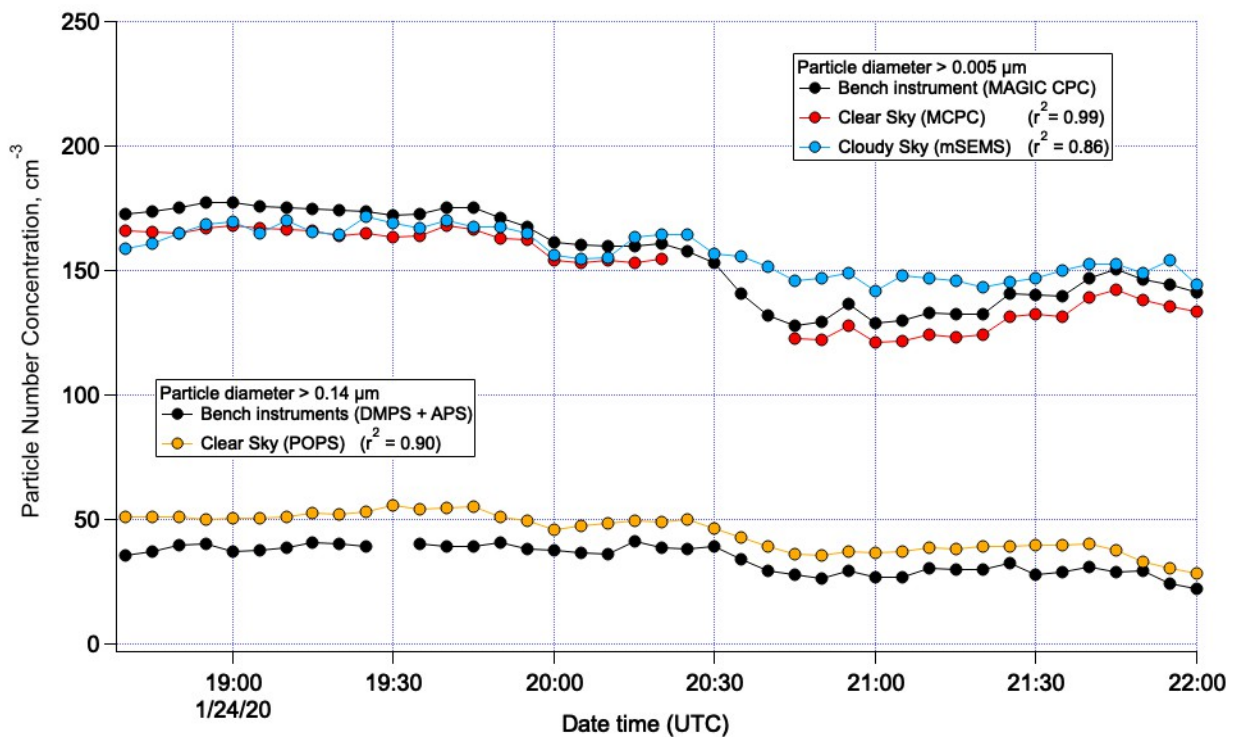
310 smaller than the overall experimental uncertainty of  $10.2 \pm 0.72\%$  indicating good agreement. A correlation between  
 311 the two measurements resulted in an  $r^2$  value of 0.86. The mSEMS was, in general lower than the MAGIC CPC for  
 312 the first half of the comparison and higher for the second half, most likely due to changes in the mSEMS inversion  
 313 routine during the experiment.

314

315 The average difference between the bench DMPS/APS and the Clear Sky POPS for diameters greater than  $0.14 \mu\text{m}$   
 316 was  $-11 \pm 7.6 \text{ cm}^{-3}$ , resulting in an average relative difference of  $-31 \pm 6.7\%$ . The overall experimental uncertainty  
 317 was  $13 \pm 0.67\%$  indicating a systemic difference resulting in consistently lower values measured by the DMPS/APS  
 318 than the POPS, again likely associated with losses in sampling lines. The  $r^2$  value for the correlation was 0.90.

319

320 *Figure 3. Comparison of particle number concentrations between bench and payload instruments for diameters*  
 321 *greater than  $0.005 \mu\text{m}$  (top half of plot) and  $0.14 \mu\text{m}$  (bottom half of plot) during ATOMIC on January 24, 2020.*  
 322 *Coefficients of determination,  $r^2$ , are for the regression between the payload CN concentration and the bench*  
 323 *instrument used for each size range.*



324

325

### 326 3.2. Absorption coefficient

327

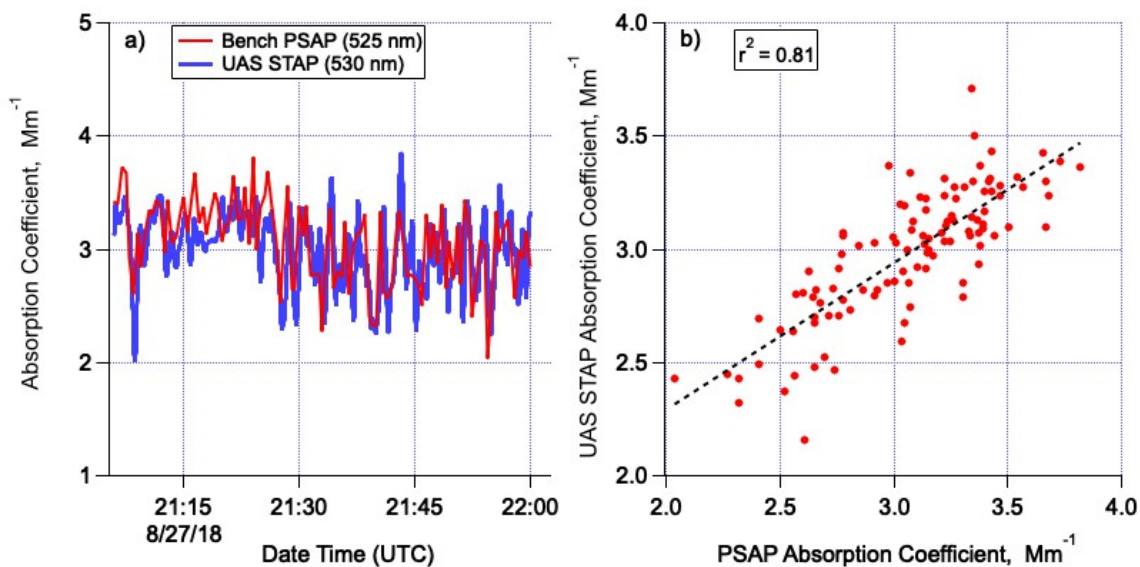
328 The Clear Sky STAP (525 nm) was compared to a Radiance Research PSAP (530 nm) at PMEL on August 27, 2018  
 329 from 21:06 to 22:00 UTC. The 5 m mast described above was used to deliver sample air to the bench top PSAP and  
 330 to the Clear Sky payload. The bench PSAP was downstream of a Berner multi-jet cascade impactor with a 50%

331 aerodynamic cut-off diameter of 1.0  $\mu\text{m}$  and a PermaPure nafion dryer (model PR-94). The Clear Sky STAP also  
332 was downstream of a PermaPure nafion dryer so that both absorption signals were measured at  $< 25\%$  RH. Data  
333 were averaged to 30 s to minimize noise. A time series of the comparison and a correlation plot are shown in Figure  
334 4a and b, respectively. The average absolute difference between the bench PSAP and the UAS STAP was  $0.11 \pm$   
335  $0.34 \text{ Mm}^{-1}$ . The average relative difference was  $3.1 \pm 12\%$ , which was smaller than the overall experimental  
336 uncertainty of  $32 \pm 3.9\%$ . The  $r^2$  value for the correlation was 0.81.

337

338 *Figure 4. Comparison of the Bench top PSAP and the Clear Sky UAS STAP as a) a time series and b) a*  
339 *correlation plot. The comparison was done of ambient air at PMEL on 8/27/18.*

340



341

342

### 343 3.3. Aerosol optical depth

344

345 Aerosol optical depth (AOD) from the miniSASP was compared to a Solar Light Microtops during Flight 5 over the  
346 Tillamook airport. The lowest altitude flown while the payload was still powered on before landing was 660 m. The  
347 miniSASP measured at 550.4 nm and the Microtops at 500 nm. The miniSASP AODs were adjusted to 500 nm  
348 using the Microtops-measured Ångstrom Exponent. Between 22:45 and 22:50 on August 11, 2022 the Microtops  
349 AOD averaged  $0.08 \pm 0.01$  while the miniSASP measured  $0.07 \pm 0.02$  indicating agreement within overall  
350 uncertainty. The lower average value for the miniSASP could be due to the higher altitude of the measurement. Due  
351 to the limited period of comparison, further tests are warranted.

352

353

354 **4. Results**

355 **4.1. First shipboard flights**

356 The first shipboard flights of the FVR-55 with payloads onboard took place from March 9 to 11, 2022 from the  
357 *TowBoatU.S. Richard L. Becker* off the coast of Key West, FL. A 6 m x 6 m launch pad was installed on the rear  
358 deck to minimize interference with boat superstructure during take-off and landing (Figure 5). A total of 11 flights  
359 were flown including 2 Functional Check Flights of the UAS, 4 with the Clear Sky payload, and 5 with the Cloudy  
360 Sky payload. The first two flights were conducted 25 miles northwest of Key West with the remainder conducted 5  
361 miles southeast of Key West. All flights were line-of-sight with a maximum altitude of 360 m due to the Certificate  
362 of Authorization (COA) in place. Unfortunately, this low flight ceiling prevented clouds from being sampled. Table  
363 4 provides a list of flights with duration, payload configuration, flight pattern, wind speed and ship heave. Wave  
364 heights during all flights were observed to be between 0.3 and 0.6 m. Ship speed was 1 to 4 m s<sup>-1</sup>.

365

366 Three flights occurred on March 10<sup>th</sup> and March 11<sup>th</sup> with both payloads being flown. With each payload in its own  
367 nose cone, swapping of payloads between flights took 30 to 45 minutes. This time included readying the plane for  
368 the next flight (installing fresh batteries and refueling).

369

370 ***Figure 5. FVR-55 with the Clear Sky payload onboard on the 6 x 6 m launch pad on the rear deck of the***  
371 ***TowBoatU.S. Richard L. Becker.***



372

373

374

375 **Table 4. Shipboard flight information including duration, payload configuration, flight pattern, wind speed, and**  
 376 **ship heave.**

Flight Number	Date	Duration (min)	Payload	Flight Pattern	Wind Speed (m s <sup>-1</sup> )	Ship heave (m)
1	3/9/23	21	FCF <sup>a</sup>		7	< 0.3
2 <sup>b</sup>	3/9/23	60	Clear	Spirals between 60 and 335 m		
3	3/9/23	62	Clear	Spirals between 60 and 335 m	5.1	< 0.3
4 <sup>c</sup>	3/10/23	5	Cloudy		4.1	0.3
5	3/10/23	17	FCF <sup>a</sup>		4.6	0.5
6	3/10/23	62	Cloudy	Circles at 335 m	4.9	0.5
7	3/10/23	60	Cloudy	Circles at 335 m	4.6	0.8
8	3/10/23	152	Clear	Circles at 120 and 335 m	2.6	0.3
9	3/11/23	183	Cloudy	Circles at 335 m	6.4	0.9
10	3/11/23	122	Cloudy	Circles at 90, 150, 210, 270, and 335 m	4.9	0.8
11	3/11/23	122	Clear	Racetracks at 150 m	5.6	0.5

377 <sup>a</sup>Functional Check Flight

378 <sup>b</sup>Telemetry file corrupted

379 <sup>c</sup>Generator failure, flight aborted

380

381 Examples of data collected during Clear and Cloudy Sky payload flights are shown in Figures 6 and 7, respectively.

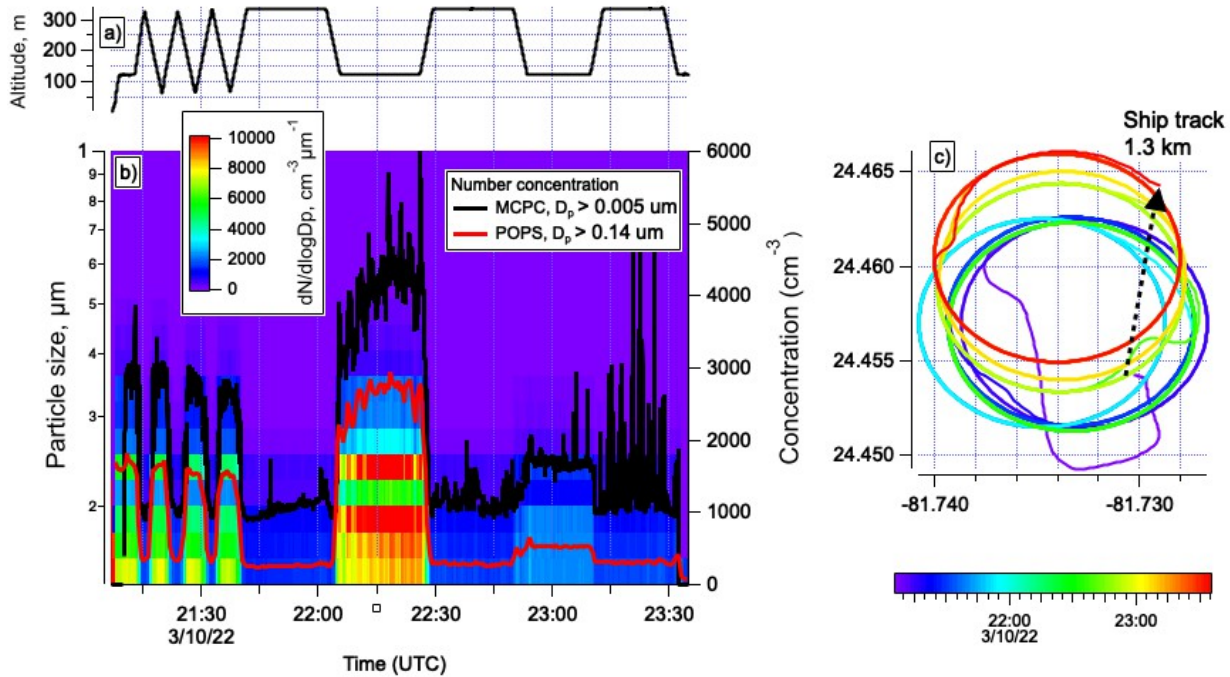
382 The Clear Sky payload was flown on Flight 8. Initially four vertical profiles between 50 and 335 m were conducted  
 383 to identify the altitude of aerosol layers. Circles were then flown alternating between 335 and 120 m (Figure 6a).

384 Particle number concentrations decreased with height, ranging up to 5,000 cm<sup>-3</sup> at 120 m and decreasing to 1000 cm<sup>-3</sup>  
 385 at 335 m for diameters greater than 0.005 μm (Figure 6b). Concentrations for diameters greater than 0.14 μm were  
 386 more than a factor of two lower. This result is expected given the large number concentration at diameters less than  
 387 0.2 μm. The flight track colored by time and the ship track are shown in Figure 6c. The ship travelled 1.3 km during  
 388 the flight. The plane landed within ± 0.36 m of the programmed spot on the launch pad.

389

390

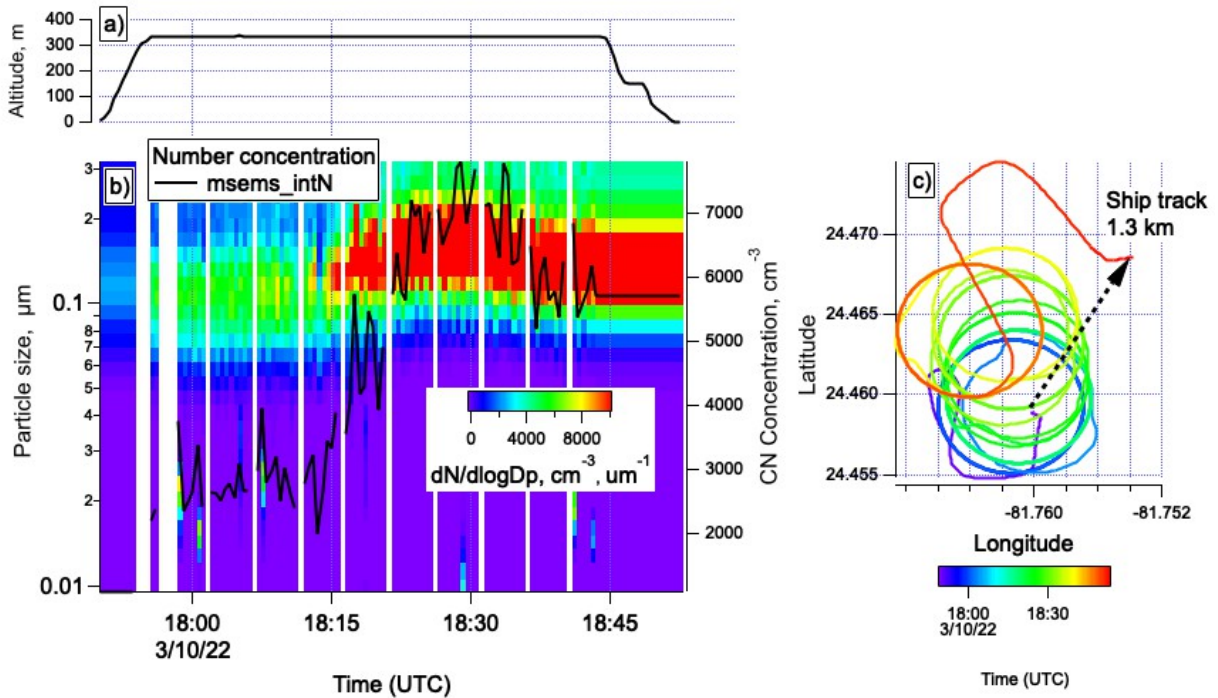
391 *Figure 6. Data from the Clear Sky payload during Flight 8 offshore of Key West including a) altitude, b) total*  
 392 *particle number concentration for two size ranges ( $D_p > 0.005$  and  $0.14 \mu\text{m}$ ) and particle number size*  
 393 *distribution, and c) the flight track colored by time along with the ship track.*  
 394



395  
 396  
 397 The Cloudy Sky payload was flown on Flight 6. After the initial ascent, circles were conducted at 335 m, the highest  
 398 altitude allowed by the COA in place (Figure 7a). Unfortunately, this altitude was below cloud bottom but the flight  
 399 served as a test of the aerosol instrumentation onboard. Initially particle number concentrations were around 3,000  
 400 cm<sup>-3</sup> but increased up to 8,000 cm<sup>-3</sup> after about 30 minutes of flight time (Figure 7b). As the number concentration  
 401 increased, the mean size of the particles shifted from about 0.12 to 0.16 μm. The flight track colored by time and the  
 402 ship track during the flight are shown in Figure 7c. The ship travelled 1.3 km during the flight with the plane landing  
 403 within ± 0.76 m of the designated spot on the launch pad.  
 404  
 405

406 *Figure 7. Data from the Cloudy Sky payload during Flight 6 offshore of Key West including a) altitude, b) total*  
 407 *particle number concentration and particle number size distribution, and c) the flight track colored by time along*  
 408 *with the ship track.*

409  
 410



411  
 412  
 413

#### 4.2. First flights in cloud

414  
 415  
 416  
 417  
 418  
 419  
 420  
 421  
 422  
 423  
 424  
 425  
 426

The FVR-55 with payloads onboard was flown from the Tillamook UAS Test Range (TUTR) in cooperation with the Near Space Corporation (NSC) between August 9<sup>th</sup> and 17<sup>th</sup>, 2022. TUTR is located at the Tillamook, OR airport about 10 km from the coast. Flights were conducted over the airport and in offshore warning areas up to 40 km from the airport under the NSC COA. Line of sight flights over the airport were conducted up to 1,370 m with the help of visual observers. For the offshore BVLOS flights, a chase plane escorted the FVR-55 through non-controlled airspace to the warning areas. NSC personnel communicated flights to the local FAA Air Traffic Control (Seattle Center) and managed airspace de-confliction. Mission Control was based out of the Tillamook airport control tower. The science team directed the Pilot-in-Control (PIC) to adjust flight tracks based on incoming, real-time data from the payloads. Five flights with the Clear Sky payload and 9 flights with the Cloudy Sky payload were conducted for a total of 38.5 flight hours (see Table 5).



427 **Table 5. TUTR flight information including duration, payload configuration, and flight pattern. Time within**  
 428 **cloud is based on a measured cloud drop number concentration above  $5 \text{ cm}^{-3}$ .**

Flight Number	Date	Duration (min)	Payload	Flight Pattern	Comments
1	8/9/12	120	Cloudy Sky	Tracks below (300 m) and within (470 m) cloud <sup>a</sup>	Over airport
2	8/9/12	123	Cloudy Sky	Tracks below (400 m) and within (530 m) cloud <sup>a</sup>	Over airport
3	8/10/12	118	Cloudy Sky	Tracks below (610 m) and within (760 to 910 m) cloud <sup>a</sup>	Over airport
4	8/10/12	119	Cloudy Sky	Tracks below (610 m) and within (910 to 980 m) cloud <sup>a</sup>	Over airport
5	8/11/22	213	Clear Sky	Chase plane escort to offshore warning area for BVLOS <sup>b</sup> flights. Orbit in aerosol layer at 2550 m.	Offshore up to ~24 NM from airport
6	8/12/22	169	Cloudy Sky	Chase plane escort to offshore warning area for BVLOS <sup>b</sup> flights. Tracks below (800 m), within (1500 m), and above (2000 m) cloud.	Offshore up to ~24 NM from airport
7	8/12/22	168	Cloudy Sky	Tracks below (910 m) and within (1000 m) cloud <sup>a</sup>	Over airport
8	8/13/22	78	Cloudy Sky	Tracks below (1300 m) and within (1370 m) cloud <sup>a</sup>	Over airport
9	8/14/22	151	Clear Sky	Orbit in aerosol layer at 2300 m.	Over airport
10	8/14/22	113	Cloudy Sky	Chase plane escort to offshore warning area for BVLOS <sup>b</sup> flights. Clouds too far away to sample.	Over airport <sup>c</sup>
11	8/15/22	223	Cloudy Sky	Chase plane escort to offshore warning area for BVLOS <sup>b</sup> flights. PIC <sup>c</sup> handoff at Netarts Beach. Tracks below (300 m), within (400 m), and above (490 m) cloud.	Offshore up to ~16 NM from airport
12	8/16/22	152	Clear Sky	Chase plane escort to offshore warning area for BVLOS <sup>b</sup> flights. PIC <sup>c</sup> handoff at Bayocean Beach. Orbit in aerosol layer at 1800 m.	Offshore up to ~16 NM from airport
13	8/16/22				Aborted. Chase plane issue.
14	8/17/22	264	Clear Sky	Orbit in aerosol layer at 1500 m.	Over airport

429 <sup>a</sup>Above cloud flights were prevented by the line of sight COA over the airport.

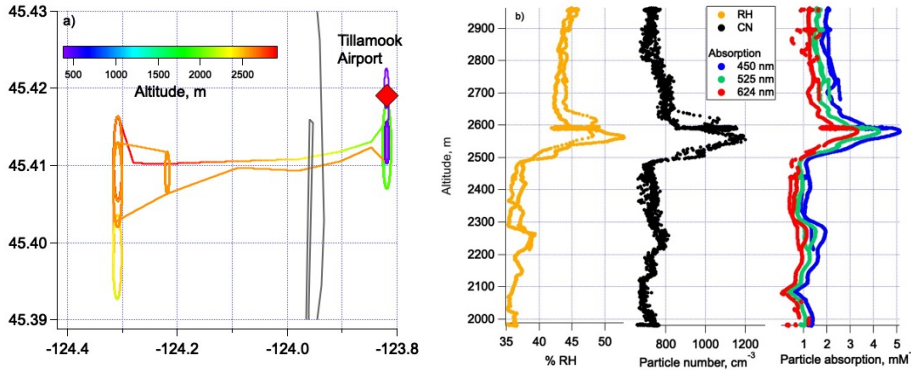
430 <sup>b</sup>Beyond visual line of sight

431 <sup>c</sup>PIC = Pilot-In-Control

432  
 433 The track from Flight 5 with the Clear Sky payload onboard is shown in Figure 8 along with vertical profiles of RH,  
 434 particle number concentration, and aerosol absorption coefficient. The presence of an aerosol layer at ~2550 m is  
 435 clear based on increased particle number concentration and aerosol absorption. The factor of 4 increase in absorption  
 436 relative to values above and below the layer indicate the aerosol was likely made up of smoke. Results from the  
 437 filter sample collected in the aerosol layer show that non-sea salt potassium, a tracer of biomass burning, was  
 438 elevated at  $0.04 \mu\text{g m}^{-3}$ . HYSPLIT trajectory analysis indicates the sampled air mass was transported northward  
 439 along the Oregon coast where several fires were burning according to the NASA FIRMS (Fire Information for

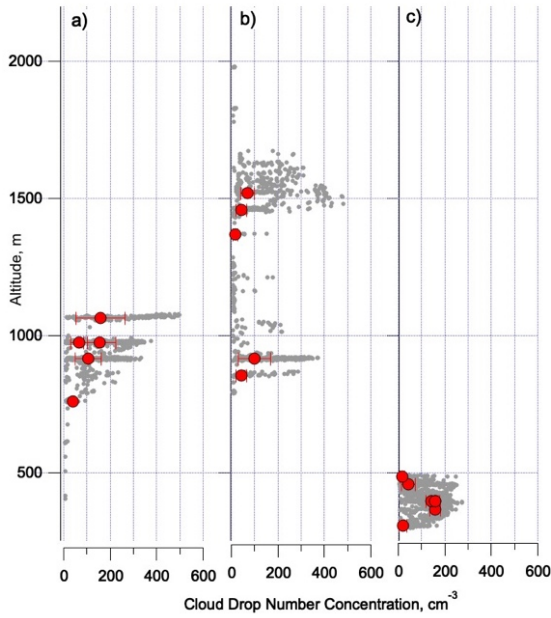
440 Resource Management System) web site ([https://firms.modaps.eosdis.nasa.gov/map/#:adv;d:today;@-](https://firms.modaps.eosdis.nasa.gov/map/#:adv;d:today;@-117.1,41.0,6.0z)  
441 117.1,41.0,6.0z).

442  
443 **Figure 8. Flight 5 track from the TUTR colored by altitude (a) and vertical profiles of RH, particle number**  
444 **concentration, and absorption coefficient (b).**



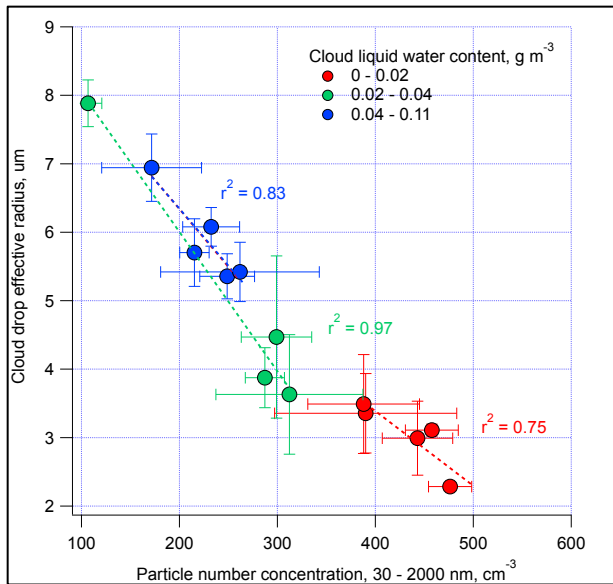
445  
446  
447 Vertical profiles of cloud drop number concentration for Flights 4, 6, and 11 are shown in Figure 9. All data points  
448 are shown in grey and level leg averaged points are shown in red. Particle number concentrations for diameters  
449 between 0.03 and 0.3  $\mu\text{m}$  were derived from the integral of the mSEMS size distribution. A lognormal fit was  
450 applied to the size distributions to extend the size range up to 2.0  $\mu\text{m}$  to encompass the entirety of the accumulation  
451 mode. The relationship between particle number concentration and cloud drop effective radius for the averaged level  
452 leg data from the three flights is shown in Figure 10. Particle number concentration and cloud drop size were well  
453 correlated ( $r^2 = 0.75$  to 0.97) for all ranges of cloud liquid water contents sampled. An increase in particle number  
454 concentration corresponded to a decrease in cloud drop size as expected for the first indirect or Twomey effect  
455 (Twomey, 1977). Future data analysis will be done to explore relationships between aerosol number concentration  
456 and size, cloud drop number concentration and size, and liquid water content for clouds at different altitudes.  
457  
458

459 **Figure 9. Vertical profiles of cloud drop number concentration for Flights a) 4, b) 6, and c) 11 from the TUTR.**  
 460 **All data points are shown in grey and level leg averaged points are shown in red.**



461  
 462  
 463  
 464  
 465  
 466  
 467  
 468

**Figure 10. Comparison of particle number concentration for diameters between 0.03 and 2.0  $\mu\text{m}$  and cloud drop effective radius averaged over the altitude level leg data shown in Figure 8. Data are binned by ranges of cloud liquid water content.**



469  
 470  
 471

472 **5.0. Conclusions**

473  
474 The initial results described here indicate that the FVR-55 UAS with Clear and Cloudy Sky payloads onboard offers  
475 a unique platform for observations relevant to aerosol direct and indirect radiative forcing. This observing platform  
476 is deployable at sea with less cost and greater flight frequency than a crewed air craft. Potential applications of this  
477 technology extend beyond aerosol – cloud observations to marine mammal assessments, harmful algal blooms, and  
478 radiative impacts from forest fires.

479  
480 Next steps include upgrading to the larger L3Harris Fixed Wing VTOL Rotator, the FVR-90. The Clear and Cloudy  
481 Sky payloads will be integrated into FVR-90 nose cones which will allow for the addition of instruments and longer  
482 flight endurance. The planned added instruments include upward and downward looking pyranometers to assess  
483 direct connections between particle number and concentration, cloud drop concentration and size, and radiation. In  
484 addition, instrumentation will be added to both payloads for the measurement of particle number size distributions  
485 from 5 nm to 3  $\mu$ m. Although larger, the FVR-90 is operable from a ship thereby fulfilling the need of aerosol,  
486 cloud, and radiation measurements in the marine atmosphere.

487  
488 **Data availability**

489 Flight data are publicly available at <https://saga.pmel.noaa.gov/Field/Tillamook2022/>.

490  
491 **Author contributions**

492  
493 PKQ and TSB designed the experiments. DJC and JEJ built and operated the payloads. LMU analyzed the chemical  
494 data. PKQ prepared the manuscript with contributions from all co-authors.

495  
496 The authors declare that they have no conflict of interest.

497  
498 **Acknowledgements**

499 We thank Aaron Farber and the entire L3Harris Latitude Engineering team for developing, fabricating, and flying  
500 the FVR-55. We thank the captain and crew of the TowBoatUS Richard L. Becker and Chuck Bagnato and Eric  
501 Waters from the Tillamook UAS Test Range for their contributions toward successful flights. We thank Alexander  
502 Smirnov of NASA GSFC for the microtops calibration, processing, and data quality assurance. We also thank  
503 NOAA OMAO and UxSRTO for logistical and financial support. This is PMEL contribution number 5537.

504  
505 **References**

506  
507 Anderson, T. L., Covert, D. S., Wheeler, J. D., Harris, J. M., Perry, K. D., Trost, B. E., Jaffe, D. J., and Ogren, J.:  
508 Aerosol backscatter fraction and single scattering albedo: Measured values and uncertainties at a coastal station in  
509 the Pacific Northwest, *Journal of Geophysical Research - Atmospheres*, 104, 26,793 - 726,807, 1999.

510 Aurell, J., Mitchell, W., Chirayath, V., Jonsson, J., Tabor, D., and Gullett, B.: Field determination of multipollutant,  
511 open area combustion source emission factors with a hexacopter unmanned aerial vehicle, *Atmospheric*  
512 *Environment*, 166, 433 - 440, 2017.

513 Bates, T. S., Coffman, D. J., Covert, D. S., and Quinn, P. K.: Regional marine boundary layer aerosol size  
514 distributions in the Indian, Atlantic and Pacific Oceans: A comparison of INDOEX measurements with ACE-1 and  
515 ACE-2, and Aerosols99, *Journal of Geophysical Research - Atmospheres*, 107, 8026, 2002.

516 Bates, T. S., Quinn, P. K., Johnson, J. E., Corless, A., Brechtel, F. J., Stalin, S. E., Meinig, C., and Burkhart, J. F.:  
517 Measurements of atmospheric aerosol vertical distributions above Svalbard, Norway, using unmanned aerial systems  
518 (UAS), *Atmospheric Measurement Techniques*, 6, 2115 - 2120, 2013.

519 Bond, T. C., Anderson, T. L., and Campbell, D.: Calibration and intercomparison of filter-based measurements of  
520 visible light absorption by aerosols, *Aerosol Science and Technology*, 30, 582 - 600, 1999.

521 Brady, J. M., Stokes, M. D., Bonnardel, J., and Bertram, T. H.: Characterization of a Quadrotor Unmanned Aircraft  
522 System for Aerosol-Particle-Concentration Measurements, *Environmental Science and Technology*, 50, 1376 - 1383,  
523 2016.

524 Chilinski, M. T., Markowicz, K. M., and Markowicz, J.: Observation of vertical variability of black carbon  
525 concentration in lower troposphere on campaigns in Poland, *Atmospheric Environment*, 137, 155 - 170, 2016.

526 Corrigan, C. E., Roberts, G. C., Ramana, M. V., Kim, D., and Ramanathan, V.: Capturing vertical profiles of aerosols  
527 and black carbon over the Indian Ocean using autonomous unmanned aerial vehicles, *Atmospheric Chemistry and*  
528 *Physics*, 8, 737 - 747, 2008.

529 Gao, R. S., Telg, H., McLaughlin, R., Ciciora, S. J., Watts, L., Richardson, M. S., Schwarz, J. P., Perring, A. E., T.D.,  
530 T., Rollins, A. W., Markovic, M. Z., Bates, T. S., Johnson, J. E., and Fahey, D. W.: A Light-Weight, High-Sensitivity  
531 Particle Spectrometer for PM<sub>2.5</sub> Aerosol Measurements, *Aerosol Science and Technology*, 50, 88 - 99, 2016.

532 Haywood, J. and Ramaswamy, V.: Global sensitivity studies of the direct radiative forcing due to anthropogenic  
533 sulfate and black carbon aerosols, *Journal of Geophysical Research - Atmospheres*, 103, 6043 - 6058, 1998.

534 IPCC: *Climate Change 2021: The Physical Science Basis* Cambridge University Press 2021.

535 Li, J., Carlson, B. E., Yung, Y. L., Lv, D., Hansen, J., Penner, J., Liao, H., Ramaswamy, V., Kahn, R., Zhang, P.,  
536 Dubovik, O., Ding, A., Lacis, A. A., Zhang, L., and Dong, Y.: Scattering and absorbing aerosols in the climate  
537 system, *Nature Reviews Earth and Environment*, 3, 363 - 379, 2022.

538 Lohmann, U. and Feichter, J.: Global indirect aerosol effects: a review, *Atmospheric Chemistry and Physics*, 5, 715 -  
539 737, 2005.

540 Murphy, D. M., Telg, H., Eck, T. F., Rodriguez, J., Stalin, S. E., and Bates, T. S.: A miniature scanning sun  
541 photometer for vertical profiles and mobile platforms, *Aerosol Science and Technology*, 50, DOI:  
542 10/1080/027/86826.2015.1121200, 2016.

543 Quinn, P. K., Coffman, D. J., Bates, T. S., Miller, T. L., Johnson, J. E., Welton, E. J., Neusüß, C., Miller, M., and  
544 Sheridan, P. J.: Aerosol optical properties during INDOEX 1999: Means, variability, and controlling factors, *Journal*  
545 *of Geophysical Research - Atmospheres*, 10.1029/2000JD000037, 2002.

546 Quinn, P. K., Thompson, E. J., Coffman, D. J., Baidar, S., Bariteau, L., Bates, T. S., Bigorre, S., Brewer, A., de Boer,  
547 G., de Szoeké, S. P., Drushka, K., Foltz, G. R., Intrieri, J., Iyer, S., Fairall, C. W., Gaston, C. J., Jansen, F., Johnson,  
548 J. E., Kruger, O. O., Marchbanks, R. D., Moran, K. P., Noone, D., Pezoa, S., Pincus, R., Plueddemann, A. J.,  
549 Pohlker, M. L., Poschl, U., Quinones Melendez, E., Royer, H. M., Szczodrak, M., Thomson, J., Upchurch, L. M.,  
550 Zhang, C., Zhang, D., and Zuidema, P.: Measurements from the RV Ronald H. Brown and related platforms as part  
551 of the Atlantic Tradewind Ocean-Atmosphere Mesoscale Interaction Campaign (ATOMIC), *Earth System Science*  
552 *Data*, 13, 1759 - 1790, 2021.

553 Rosenfeld, D., Zhu, Y., Wang, M., Zheng, Y., Goren, T., and Yu, S.: Aerosol-driven droplet concentrations dominate  
554 coverage and water of low-level clouds, *Science*, 363, 10.1126/science.aav0566, 2019.

555 Russell, P. B., Hobbs, P. V., and Stowe, L. L.: Aerosol properties and radiative effects in the United States East Coast  
556 haze plume: An overview of the Tropospheric Aerosol Radiative Forcing Observational Experiment (TARFOX),  
557 *Journal of Geophysical Research - Atmosphere*, 104, 2213 - 2222, 1999.

558 Takemura, T., Nakajima, T., Dubovik, O., Holben, B. N., and Kinne, S.: Single-scattering albedo and radiative  
559 forcing of various aerosol species with a global three-dimensional model, *Journal of Climate*, 15, 333 - 352, 2002.

560 Telg, H., Murphy, D. M., Bates, T. S., Johnson, J. E., Quinn, P. K., Giardi, F., and Gao, R. S.: A practical set of  
561 miniaturized instruments for vertical profiling of aerosol physical properties, *Aerosol Science and Technology*, 51,  
562 715 - 723, 2017.

563 Twomey, S.: The influence of pollution on the shortwave albedo of clouds, *Journal of Atmospheric Science*, 34,  
564 1149 - 1152, 1977.

565 Yoon, S.-C. and Kim, J.: Influences of relative humidity on aerosol optical properties and aerosol radiative forcing  
566 during ACE-Asia, *Atmospheric Environment*, 40, 4328 - 4338, 2006.

567 Zhang, Y., Forrister, H., Liu, J., Dibb, J., Anderson, B., Schwarz, J., Perring, A. E., Jimenez, J., Campuzano-Jost, P.,  
568 Wang, Y., Nenes, A., and Weber, R. J.: Top-of-atmosphere radiative forcing affected by brown carbon in the upper  
569 troposphere, *Nature Geoscience*, 10, 486 - 489, 2017.

570